CORROSION SCIENCE AND TECHNOLOGY, Vol.23, No.2(2024), pp.93~103 pISSN 1598-6462 / eISSN 2288-6524
[Research Paper] DOI: https://doi.org/10.14773/cst.2024.23.2.93

Phase-Field Modelling of Zinc Dendrite Growth in ZnAlMg Coatings

Mikel Bengoetxea Aristondo[1,†], Kais Ammar[1], Samuel Forest[1], Vincent Maurel[1], Houssem Eddine Chaieb[2], and Jean-Michel Mataigne[3]

[1]*Mines Paris-PSL University, Centre des Matériaux, CNRS UMR 7633, Evry, BP 87 91003, France*
[2]*OCAS NV, President John F. Kennedylaan 3, 9060, Zelzate, Belgium*
[3]*ArcelorMittal Global R&D, Voie Romaine, 57280, Maizières-lès-Metz, France*
(Received January 12, 2024; Revised February 08, 2024; Accepted February 08, 2024)

In the present work, a phase-field model for dendritic solidification is applied to hot-dip ZnAlMg coatings to elucidate the morphology of zinc dendrites and the solute segregation leading to the formation of eutectics. These aspects define the microstructure that conditions the corrosion resistance and the mechanical behaviour of the coating. Along with modelling phase transformation and solute diffusion, the implemented model is partially coupled with the tracking of crystal orientation in solid grains, thus allowing the effects of surface tension anisotropy to be considered in multi-dendrite simulations. For this purpose, the composition of a hot-dip ZnAlMg coating is assimilated to a dilute pseudo-binary system. 1D and 2D simulations of isothermal solidification are performed in a finite element solver by introducing nuclei as initial conditions. The results are qualitatively consistent with existing analytical solutions for growth velocity and concentration profiles, but the spatial domain of the simulations is limited by the required mesh refinement.

Keywords: *ZnAlMg coatings, Dendritic solidification, Phase-field model, Crystal orientation*

1. Introduction

Corrosion protection is often a major requirement of steel structures and, traditionally, zinc-rich metallic coatings have been used to cover steel sheets to this effect. In fact, zinc provides galvanic protection to the steel substrate. This protection must be combined with an appropriate mechanical behaviour, so that corrosion do not reach steel by coating decohesion or cracking. Consequently, the balance between anticorrosive and mechanical properties, as well as other factors such as lightweighting and cost reduction, condition the optimisation approaches of these coatings. In this sense, ZnAlMg coatings have created great interest in industry.

1.1 ZnAlMg coatings

Provided that the additions of aluminium and magnesium do not change the primary phase to be other than zinc, the microstructure of ZnAlMg coatings is composed of zinc dendrites surrounded by binary and ternary eutectics [1,2]. The main contributions of adding aluminium to the zinc bath are its inherent passivation [3], and the formation of Fe-Al or Fe-Al-Zn intermetallic compounds at the substrate-coating interface, instead of brittle layers of Fe-Zn intermetallic compounds [4,5]. As for magnesium additions, corrosion resistance is improved because anodic reactions happen preferentially in phases containing this element and its corrosion products are especially protective [6-8]. Nonetheless, the influences of these and other alloying elements in mechanical behaviour and corrosion are not thoroughly understood, which is necessary to set the relations between microstructure and in-service response.

Regarding corrosion aspects, Osório *et al.* concluded that there are three key factors in zinc-rich coatings [6]: the elements in the alloy, their electrochemical behaviour and the solidification cooling rate. The latter can alter the phase fractions in the microstructure and, more importantly, high cooling rates promote the nucleation of primary dendrites resulting in finer microstructures with more atoms in solution. In general, finer microstructures are considered to be less corrosion resistant, since grain boundaries act as corrosion initiation sites due to the presence of defects, plastic deformation and segregated

[†]Corresponding author: mikel.bengoetxea_aristondo@minesparis.psl.eu

impurities [6,9-11]. Nevertheless, Osório *et al.* found that the secondary dendrite arm spacing and the hypoeutectic or hypereutectic nature of ZnAl alloys play also a major role in corrosion resistance [6].

Similarly, it has often been observed that magnesium prevents intergranular corrosion despite making microstructure finer [8,12,13]. In fact, magnesium has a more negative electrode potential than zinc and aluminium ($E_{Mg} < E_{Zn} < E_{Al}$), so a fine microstructure facilitates the precipitation of its corrosion products in cathodic phases. This helps to keep acidity more uniform all over the surface and micro-galvanic coupling between different phases is also reduced [8], which results in a less intense and more uniform corrosion attack. Nonetheless, the values of electrode potentials can be inversed depending on environmental conditions such as acidity and temperature. For example, Prosek *et al.* observed that aluminium phases activate and dissolve before zinc in alkaline environments for Zn5.1Al (wt%) [8]. These studies demonstrate that phase fractions, their morphologies and solute distributions condition the corrosion behaviour of ZnAlMg microstructures, with the alloying elements and the solidification process being decisive factors. The same holds for the mechanical behaviour of these coatings, given the diversity of microconstituents and their different properties [1,2,9].

1.2 Phase-field modelling of dendritic growth

Phase-field models are known to be efficient in solving solidification problems, by representing that the liquid-solid transformation occurs continuously across an interface of finite thickness [14]. This method offers the possibility to simulate solidification morphologies and, when it is coupled with diffusion equations, solute concentration fields are also obtained. According to the previous section, this information and thus phase-field models are of great interest to understand and predict the microstructures of zinc-rich coatings, as well as their mechanical and corrosion properties. In particular, a model for isothermal dendritic solidification of dilute binary alloys proposed by Karma *et al.* has been extensively developed since the 1990s [15-17]. The main advantage of this formulation is the decoupling of bulk and interfacial energies in equilibrium, by considering the equality of chemical potentials on both sides of the solid-liquid interface [18] and by assuming linear liquidus and solidus. Results of numerical simulations for various materials can be found in literature [19,20]. As for ZnAlMg coatings, Kim *et al.* studied the morphology of zinc dendrites in Zn0.2Al coatings by considering three preferential growth directions (<$10\bar{1}0$>, <0001> and the directions normal to the {$\bar{1}2\bar{1}1$} planes) [21]. Regarding multiphase multicomponent models, De Bruycker *et al.* simulated Zn5Al and Zn4Al2Mg microstructures [22] and Mogeritsch *et al.* carried out simulations for Zn2.5Al1.5Mg [23]. Aiming at large scale multi-dendrite simulations, adaptive meshing [24] and non-linearly preconditioned formulations [25] have been applied to reduce the computational cost. Several proposals for tracking the crystal orientation can also be found: local front tracking [25,26], and variations of the KWC model [27,28] with different formulations of the orientational energy [29,30].

The aim of this study is to develop a phase-field model for hot-dip ZnAlMg coatings, focusing on the simulation of multiple primary zinc dendrites. Given that this family of coatings often exhibits a pronounced basal texture and that dendrite branches typically span the entire thickness of the coating [12,31], the main simulations presented in this study are 2D simulations in a plane parallel to the substrate-coating interface, with the c-axis of the hexagonal close-packed (HCP) lattice oriented perpendicular to the simulation plane. Only <$10\bar{1}0$> directions are therefore considered as preferential growth directions, which implies 6-fold dendrites. The phase-field model adopted is that developed by Karma *et al.* [15,16], so the ZnAlMg system is treated as a pseudo-binary system where the alloying elements are considered as a unique chemical species. The tracking of crystal orientation is done by adopting the energy formulation of Henry *et al.* [29] and implementing a partial coupling with the phase-field equations. The composition of the coating used in the simulations is Zn4.67Al0.43Mg.

2. Phase-field Modelling

2.1 Phase-field and diffusion equations

The model proposed by Karma *et al.* [15,16] deals with the dendritic solidification of binary alloys, where

two variables are considered: the order parameter φ and the solute concentration c. The former varies between -1 and 1, which correspond to the values in the liquid and solid bulk, respectively. The latter varies between 0 and 1, and corresponds to the atomic fraction of solute. Both variables are dimensionless. Temperature T could also be considered as a variable by adding the corresponding thermal diffusion equation [17], but temperature is considered as an externally imposed constant parameter in this study concerning isothermal solidification.

The first step to build the phase-field model is the formulation of the free energy functional F, which is often represented as follows (A refers to the main element and B to the solute elements):

$$\begin{aligned} F(\varphi, \nabla\varphi, c, T) &= \int_V f(\varphi, \nabla\varphi, c, T)dV \\ &= \int_V \left[\frac{\sigma}{2}\|\nabla\varphi\|^2 + f_H(\varphi) + f_{AB}(\varphi, c, T)\right]dV \end{aligned} \quad (1)$$

The first two terms of the integral in equation (1) correspond to the interfacial energy and the third one corresponds to the bulk energy. The bulk energy of each phase (f_L for liquid and f_S for solid) can be obtained from thermodynamic databases, and in this model its value depends on c and T. When there are several phases in the system, the bulk energy of the system also depends on the phase fractions, so in the case of solidification, $f_{AB}(\varphi, c, T)$. Regarding interfacial energy, $f_H(\varphi)$ corresponds to a double-well potential that links the bulk energies of the liquid and solid phases, by ensuring that equilibrium can be reached in both phases. For example, $f_H(\varphi) = H(-\varphi^2/2 + \varphi^4/4)$, where H is the height of the energy barrier between the two phases. The phase-field gradient term $\sigma\|\nabla\varphi\|^2/2$ in equation (1) is a penalty factor for the transition between phases to ensure a finite interface thickness, where σ is a coefficient in which anisotropy aspects can be introduced.

In the case of a dilute binary alloy, the following expression can be deduced for the free energy density of the system by assuming linear liquidus and solidus curves, and equal chemical potentials on both sides of the solid-liquid interface [14,16]:

$$\begin{aligned} f(\varphi, \nabla\varphi, c, T) &= \frac{3W\gamma}{4\sqrt{2}}\|\nabla\varphi\|^2 + \frac{3\gamma}{2\sqrt{2}W}\left(\frac{-\varphi^2}{2} + \frac{\varphi^4}{4}\right) + f_{LA}(T_{mA}) \\ &-(T - T_{mA})\left\{s_{LA} - \frac{L_A}{2T_{mA}}\left[1 + \frac{15}{8}\left(\varphi - \frac{2\varphi^3}{3} + \frac{\varphi^5}{5}\right)\right]\right\} \\ &+ c(T_{mB} - T_{mA})\left\{ s_{LB}\right. \\ &\left. -\frac{L_B}{T_{mB}\ln(k)}\ln\left[\frac{1}{2} + \frac{k}{2} - \frac{15}{16}\left(\varphi - \frac{2\varphi^3}{3} + \frac{\varphi^5}{5}\right)(1-k)\right]\right\} \\ &+ \frac{RT_{mA}\rho}{P}[c\ln(c) - c] \end{aligned} \quad (2)$$

where W is a length proportional to the interface thickness, γ is the interfacial energy, T_{mi} is the melting point of the chemical element i, f_{LA} is the bulk free energy density of A in the liquid phase, s_{Li} is the entropy value of i in the liquid phase, L_i is the latent heat of i, ρ is the mass density, P is the molar mass, R is the ideal gas constant, and k is the partition coefficient which is the ratio between the equilibrium solute concentrations in the solid and liquid phases (c_{S0}/c_{L0}). Under equilibrium conditions, the evaluation of interfacial energy yields into $\gamma = \text{IWH}$ where $I = 2\sqrt{2}/3$.

The next step is to develop the evolution equations of φ and c. The non-conserved variable φ evolves with the time-dependent Ginzburg-Landau equation (3), whereas the conserved variable c is governed by the mass balance equation of solute (4):

$$\frac{\partial\varphi}{\partial t} = -Q\frac{\delta F(\varphi, \nabla\varphi, c)}{\delta\varphi} \quad (3)$$

$$\frac{\partial c}{\partial t} = \nabla\cdot\left[M(\varphi, c)\nabla\frac{\partial F(\varphi, \nabla\varphi, c)}{\partial c}\right] \quad (4)$$

where Q is the kinetic constant and $M(\varphi,c)$ is the mobility of solute. Crystal anisotropy is introduced in the interfacial energy [32] and, since $\nabla\varphi/\|\nabla\varphi\|$ is the normal unit vector of the solid-liquid interface, surface tension anisotropy can be introduced by considering $\gamma(\nabla\varphi)$, with the most common option being to consider $W(\nabla\varphi)$ and keep H isotropic [32]. The anisotropy of attachment kinetics is not considered in this study [31], because a 6-fold symmetry is enough to consider only $<10\bar{1}0>$ directions as preferential:

$$\begin{aligned} W(\nabla\varphi) &= W_0[1 + \varepsilon_c\cos(6\alpha)] \\ &= W_0[1 + \varepsilon_c(2n_x^6 - 12n_x^4n_y^2 + 18n_y^4n_x^2 - 1)] \end{aligned} \quad (5)$$

where W_0 is the isotropic "interface thickness", ε_c is the anisotropy coefficient, $n_i = \varphi_i'/\|\nabla\varphi\|$ are the components of the normal unit vector of the solid-liquid interface expressed in terms of the gradient and partial derivatives of φ with respect to X- and Y-axes, and $\alpha = \arctan(\varphi_y'/\varphi_x')$ is the angle between this normal unit vector and the X-axis, by assuming that 2D simulations are done in the X-Y plane. The combination of equations (1), (3) and (4) leads to the following evolution equation:

$$0 = -\tau\frac{\partial\varphi}{\partial t} + \nabla\cdot\left[W(\nabla\varphi)\frac{\partial W(\nabla\varphi)}{\partial\nabla\varphi}\|\nabla\varphi\|^2 + W^2(\nabla\varphi)\nabla\varphi\right] + \varphi - \varphi^3 - \frac{\lambda}{1-k}\left[\frac{c}{c_0(\varphi)} - 1\right](1-\varphi^2)^2 \quad (6)$$

where $\tau = 1/(QH)$ is the phase-field relaxation time, λ is the interface-bulk coupling parameter and $c_0(\varphi)$ is the equilibrium concentration profile.

$$\lambda = \frac{15RT_{mA}(1-k)^2 c_{L0}\rho}{16HP} \quad (7)$$

$$c_0(\varphi) = \frac{c_{S0} + c_{L0}}{2} + \varphi\frac{c_{S0} - c_{L0}}{2} \quad (8)$$

$$c_{S0} = k\,c_{L0} = k\left(c_{nom} + \frac{T_{liquidus} - T}{|m|}\right) \quad (9)$$

where m is the slope of the liquidus, c_{nom} is the nominal solute concentration of the coating and $T_{liquidus}$ is its liquidus temperature. As for the evolution of c, $M(\varphi, c)$ is related to the diffusion coefficients D_L and D_S (liquid and solid, respectively) and the development of equation (4) leads to:

$$\frac{\partial c}{\partial t} = \nabla\cdot\left\{\left(D_L\frac{1-\varphi}{2} + D_S\frac{1+\varphi}{2}\right)\frac{c}{c_0(\varphi)}\left[\frac{\nabla c}{c} + \frac{(1-k)c_{L0}\nabla\varphi}{2c_0(\varphi)}\right]\right\} \quad (10)$$

It is common to artificially scale up the value of W, which is a layer of some atoms of the order of 10^{-10} m [18]. In this way, non-equilibrium effects are magnified at the interface and, to diminish them, the interpolation functions of the model are chosen according to asymptotic analysis. A correction called "anti-trapping current" is also usually applied [16], but it has been neglected in this study. Some other relations derived from asymptotic analysis are the following ones [15,16]:

$$\tau = \lambda W\left(\frac{\beta}{a_1} + a_2\frac{W}{D_L}\right) \quad (11)$$

$$\frac{W}{d_0} = \frac{\lambda}{a_1} \quad (12)$$

where β is the kinetic coefficient neglected in this study, d_0 is the capillary length defined as $d_0 = \gamma P/[T_{mA}R(1-k)^2\rho c_{L0}]$, and $a_1 = 5\sqrt{2}/8$ and $a_2 = 47/75$ according to asymptotic analysis.

2.2 Tracking of crystal orientation

Nucleation models assign specific crystal orientations to nuclei (in general, one angle θ in 2D simulations where only <10$\bar{1}$0> directions are considered as preferential growth directions) and growth models take them into account, since each dendrite grows according to its crystal orientation. For the sake of simplicity, the liquid phase is assumed to have a uniform reference value or random values of crystal orientation. There are therefore two aspects that the solidification phase-field model must include: the crystal orientation of each point must be tracked according to the dendrite to which it belongs, and the solution of the evolution equations must consider the local crystal orientation to apply anisotropy relations. Thus, equation (5) becomes $W = W_0\{1 + \varepsilon_c\cos[6(\alpha - \theta)]\}$, where θ represents a rotation of the c-axis of the HCP lattice in the X-Y plane.

In this sense, an orientational energy term could be added to the free energy functional F in equation (1), to account for the effect of grain boundaries [27,28]. In this study, this additional term is not considered because dendritic growth is expected to slow down during eutectic solidification, and contacts between dendrites should therefore be rare. Consequently, no orientational energy term is added to solve equations (3) and (4), and the partial derivative of W with respect to θ is neglected. However, the crystal orientation θ is tracked according to the orientational energy density form proposed by Henry *et al.* [29] and an evolution equation of the Ginzburg-Landau form:

$$f_{ori} = H_\theta p(\varphi)(\nabla\theta)^2 \quad (13)$$

$$\frac{\partial\theta}{\partial t} = -M_\theta(\varphi)\frac{\delta F(\varphi, \nabla\theta)}{\delta\theta} = M_\theta(\varphi)\nabla\cdot[2H_\theta p(\varphi)\nabla\theta] \quad (14)$$

where H_θ is a constant of proportionality, $p(\varphi)$ is an

interpolation function between the liquid and solid phases and $M_\theta(\varphi)$ is the associated mobility. $M_\theta(\varphi)$ and $p(\varphi)$ are chosen so that $M_\theta(\varphi)$ be zero in the solid phase and $p(\varphi)$ be zero in the liquid phase, tending to infinity in the other phase:

$$p(\varphi) = \frac{2(\varphi+1)^3}{(\varphi-1)^2} \tag{15}$$

$$M_\theta(\varphi) = M_0\frac{2(\varphi-1)^2}{(\varphi+1)^2} \tag{16}$$

To solve equation (14), only the orientational energy density term is considered in the free energy functional, and both partial derivatives with respect to φ and $\nabla\theta$ are calculated. The evolution of crystal orientation is therefore partially coupled to the phase-field equation, i.e. θ is tracked to correctly apply surface tension anisotropy during dendritic growth, without affecting the evolution of phase transformation and diffusion.

3. Finite Element Simulations and Discussion of Results

3.1 Choice of parameters

The input parameters for the simulations of Zn4.67Al0.43Mg are detailed in Table 1. The rest of the parameters are calculated using the relations given in the previous section, except for the temperature T and the "interface thickness" W, which are chosen to set a certain thermal undercooling and to manage numerical aspects, respectively. The thermal undercooling is set to 10 ºC for 1D simulations and to 20 ºC for 2D simulations. The space and time factors used to adimensionalise the equations are W_0 and τ. The simulations are performed in a uniformly meshed domain of quadrangle linear elements, with zero-flux boundary conditions for φ, c and θ.

Table 1. Input parameters of the model

Parameter	Value	Units	Source
k	0.233	-	Estimated from COST507 [33]
c_{nom}	11.62	at.%	-
m	-364	K	Estimated from COST507 [33]
D_L	$2\cdot10^{-9}$	m^2/s	Estimated from [34]
D_S	0.0	m^2/s	-
ε_c	0.1	-	-
ρ	6350	kg/m^3	Estimated from [35]
$T_{liquidus}$	650.5	K	Estimated from COST507 [33]
P	63.41	g/mol	-
γ	0.09	J/m^2	Estimated from [36,37]
H_ϑ	$5.17\cdot10^6$	J/m	-
M_0	4.71	$m^3/(J\ s)$	-

3.2 1D simulations

1D simulations are performed to assess the correspondence between the numerical results of the phase-field model and the analytical solutions for steadily growing planar precipitates [38]. The grid size is set to $\Delta x = 0.5W_0$ and the total length of the simulation domain is $500W_0$, where W_0 is defined for each simulation so that $W_0/d_0 = 10$. In the initial state, a nucleus of size $5W_0$ is placed on one side of the system and the evolution of the solid-liquid interface, as well as the concentration profile are tracked along the simulation. Three values of the initial supersaturation Ω_c are tested ($\Omega_{c1} = 0.25$, $\Omega_{c2} = 0.78$ and $\Omega_{c3} = 0.95$) and, according to equation (18), each of these values is associated with an initial nominal concentration of the liquid phase ($c_{nom1} = 0.116$, $c_{nom2} = 0.058$ and $c_{nom3} = 0.039$).

The growth velocity of the solid phase is evaluated by measuring the displacement in time of the solid-liquid interface at $\varphi = 0$, and its analytical expression is as follows [38]:

$$v(t) = \frac{\lambda_c\sqrt{D_L}}{2\sqrt{t}} \tag{17}$$

where λ_c is calculated from Ω_c:

$$\Omega_c = \frac{c_{nom}-c_{L0}}{c_{S0}-c_{L0}} = \frac{\sqrt{\pi}}{2}\lambda_c\exp\left(\frac{\lambda_c^2}{4}\right)erfc\left(\frac{\lambda_c}{2}\right) \tag{18}$$

Fig. 1 shows the numerical and analytical results of the growth velocity for the three supersaturation values. The convergence of the simulation results was checked for different Δx and W_0/d_0 values, as illustrated by the simulation results for $\Delta x = 0.25W_0$ and $W_0/d_0 = 5$ in the case of Ω_{c1}. The numerical results are fitted with curves of type $A/\sqrt{t}$ where A is a constant coefficient, and an

increase in velocity is observed when the value of Ω_c is increased in both numerical and analytical results. This corroborates that supersaturated systems are further from thermodynamic equilibrium. Nonetheless, the numerical and analytical results do not match quantitatively, leading to errors of $e_1 = 4.5 \cdot 10^{-4}$ m/s, $e_2 = 2.9 \cdot 10^{-3}$ m/s and $e_3 = 10^{-2}$ m/s between the fit curves and the analytical results at the end of the simulations. These differences are reasonable since the analytical solution does not consider temperature effects. In the case of Ω_{c2} and Ω_{c3}, the marked drops in the growth velocities by the end of the simulations are boundary effects due to the limited simulation domain.

Profiles of solute concentration can also be tracked and analytically calculated. Their evolution in the liquid phase is given by the following expression [20]:

$$c(x,t) = c_{nom} + (c_{L0} - c_{nom}) \frac{erfc\left\{\dfrac{\lambda_c [x(t) - x_0(0)]}{2[x_0(t) - x_0(0)]}\right\}}{erfc\left(\dfrac{\lambda_c}{2}\right)} \quad (19)$$

where $x(t)$ is the spatial coordinate, $x_0(t)$ is the position of the solid-liquid interface at time t, and $x_0(0)$ is the position of the solid-liquid interface in the initial state. Fig. 2 compares the results of two simulations with this analytical solution at different moments of the simulations. As the results correspond to the liquid phase, the initial values of these curves are the concentration peaks at the solid-liquid interface. The lower the value of Ω_c is, the closer to the interface the concentration in the liquid reaches its bulk value with respect to the analytical solution. In addition, the numerical peak concentrations

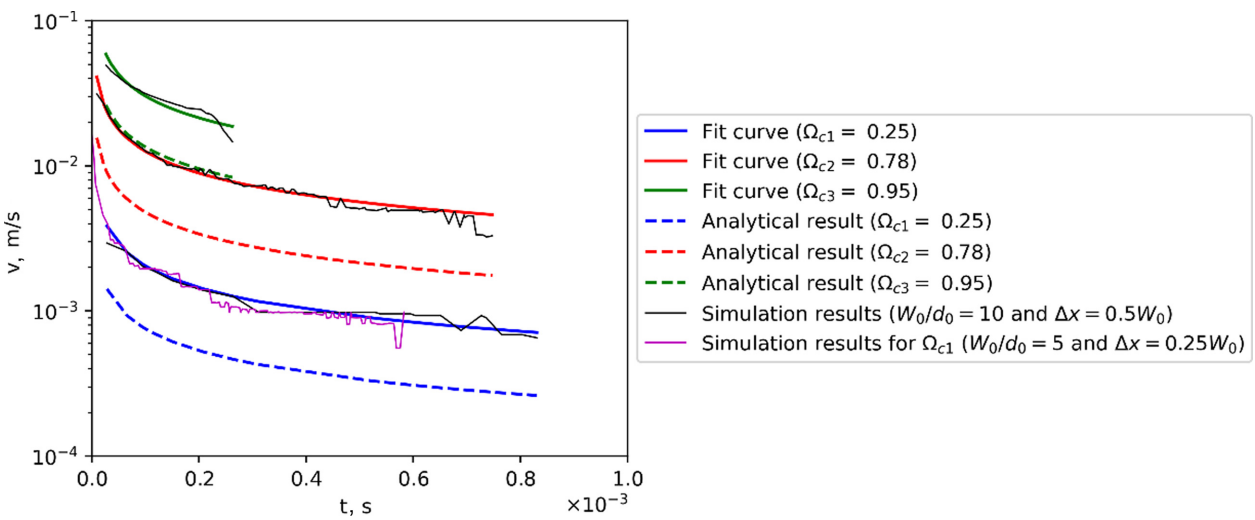

Fig. 1. Profiles of growth velocity for different supersaturation values

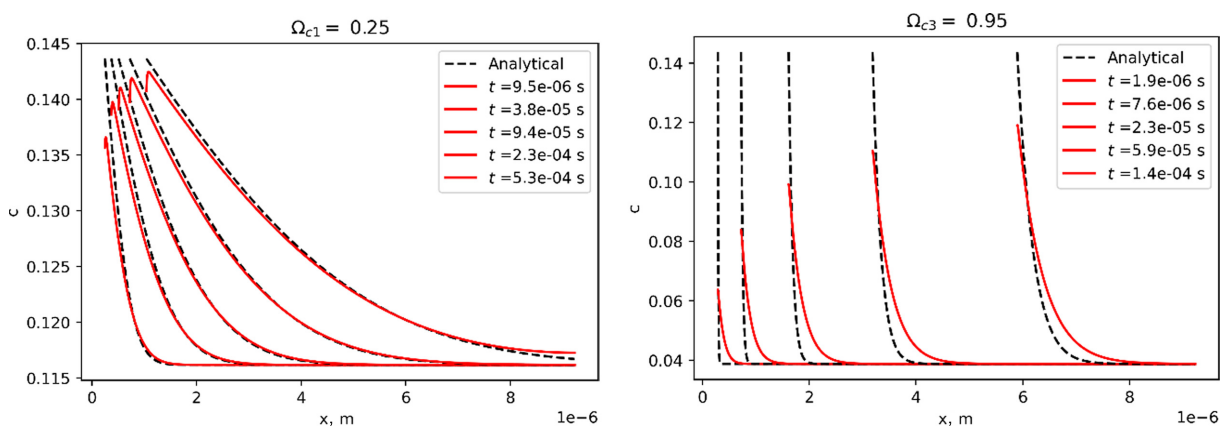

Fig. 2. Profiles of solute concentration in the liquid for different supersaturation values

become higher with time, while the analytical peak concentrations remain constant because the concentration at the solid-liquid interface is a fixed boundary condition in [38]. The curves affected by boundary effects are not shown in this case, because the analytical expression is no longer valid.

3.3 Isothermal dendritic solidification

Quarters of dendrites are simulated in a 2D mesh, conveniently oriented to take advantage of the 6-fold symmetry (the first branch grows at 30º from the X-axis and the second at 90º). The "interface thickness" W_0 is fixed at 15.5 nm so that $W_0/d_0 = 10$, and the inserted nuclei have a radius of $4W_0$. The convergence of the results is examined by varying the grid size Δx between 0.25 W_0 and 1.5 W_0. Fig. 3 shows the fields φ and c of the simulation corresponding to $\Delta x = W_0$, where segregation of solute in the liquid near to the solid-liquid interface is visible. This simulation of 502,002 degrees of freedom was run in 20 cores and took 3.4 days of wall-clock time. The simulation domain is limited to a total size of 7.75 × 7.75 μm^2 due to the high computational cost. Hence, the results of this study represent only the first growth stage of zinc dendrites, which actually have a total size of a few tens of microns.

The growth velocities of the primary branches in directions <10$\bar{1}$0> can be evaluated by measuring the displacement in time of the points where $\varphi = 0$. When comparing these dendrite tip velocities for different Δx in Fig. 4, it is observed that the values of different branches converge when Δx is below $0.5W_0$. Thus, growth velocity becomes independent of grid anisotropy and discretization around this element size. Due to the sudden thermal undercooling of 20 ºC, the velocities

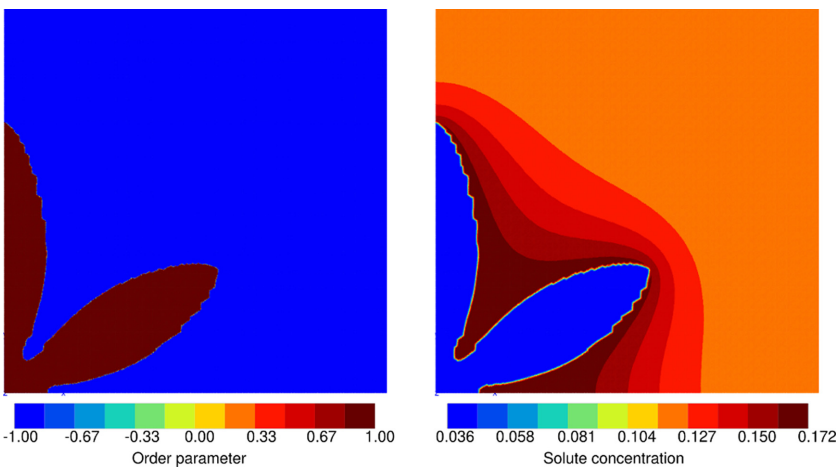

Fig. 3. Phase field φ (left) and concentration field c (right) of isothermal simulation ($t = 499\tau = 0.33$ ms)

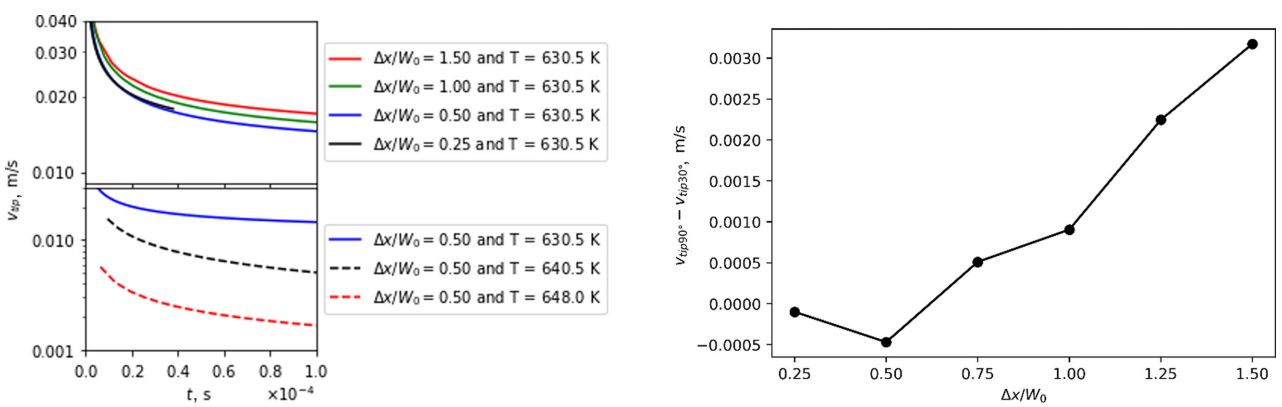

Fig. 4. Fitted tip velocity curves of type A/$\sqrt{t}$ + B for dendrite branch at 90º (left), and differences in fitted tip velocities between the branches at 30º and 90º at the end of the simulations for different Δx (right)

obtained are 1-2 orders of magnitude higher than those calculated for a galvanising test machine [39]. The dashed curves in Fig. 4 correspond to simulations for lower undercoolings (T = 640.5 K and T = 648 K), where a drastic reduction in dendrite tip velocity is observed. The results should therefore be close to reasonable values in the case of realistic thermal paths.

In order to assess the concentration profiles, the solute concentrations along the dendrite branches are compared with the values obtained by the Gibbs-Thomson relation without the kinetic term. In fact, as no diffusion is considered in the solid phase, the concentration on the solid side of the interface obtained from equation (20) corresponds to the final concentration in the solid:

$$\frac{c_S}{c_{L0}} = k\left(1 - \frac{(1-k)d_0}{\rho_{tip}}\right) \tag{20}$$

where the dendrite tip radius ρ_{tip} is calculated from simulation results according to Vakili *et al.* [40] (a negative sign is added to obtain positive tip radii in the solid-to-liquid direction):

$$\frac{1}{\rho_{tip}} = -\frac{1}{\|\nabla\varphi\|}\left(\nabla^2\varphi - \frac{\nabla\varphi\cdot\nabla\|\nabla\varphi\|}{\|\nabla\varphi\|}\right) \tag{21}$$

This implies that the c_S value obtained from equation (20) is not completely analytical, but it serves as a reference for comparison. For example, Fig. 5 shows the concentration profile along a dendrite branch for $\Delta x = W_0$, where the mean absolute error of the simulation result with respect to the semi-analytical result from the Gibbs-Thomson relation is 0.028 at.%. The detail in Fig. 5 shows that the semi-analytically obtained concentration is lower than the concentration profile for a flat solid-liquid interface where ρ_{tip} tends to infinity ($c_{S0} = k\,c_{L0}$), which is the effect of introducing a positive curvature in the Gibbs-Thomson relation. The semi-analytical concentration is also lower than the simulation result, and this difference is most likely due to solute trapping

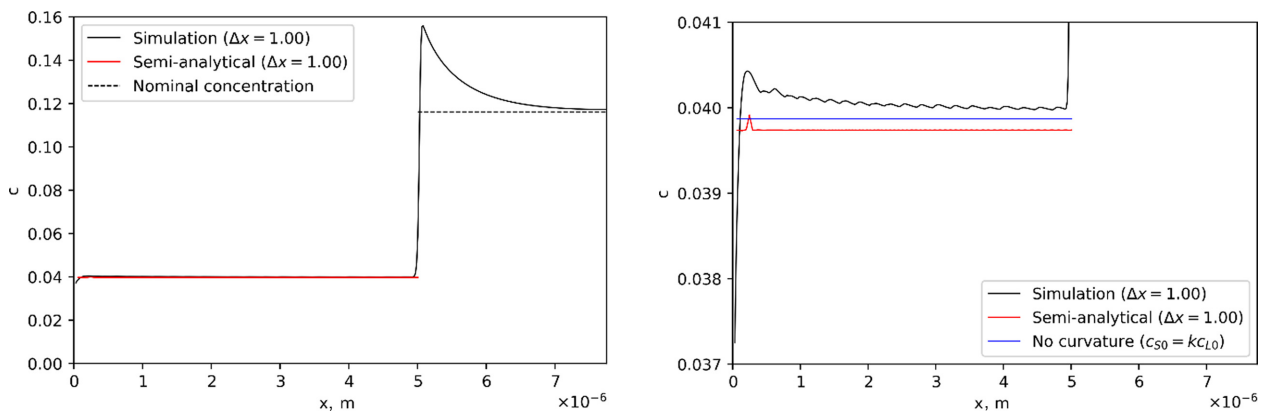

Fig. 5. Solute concentration profile along a dendrite branch (left) and its detail of the solid portion (right)

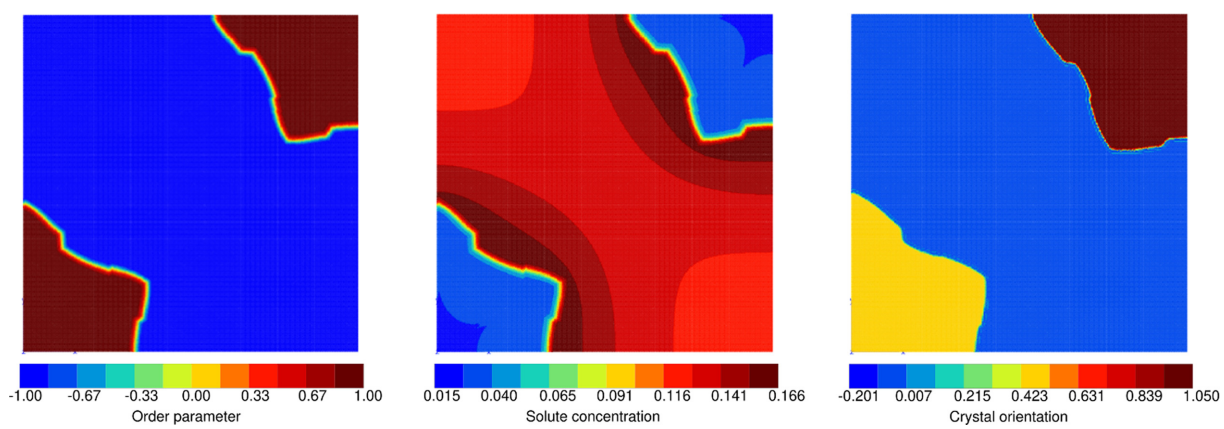

Fig. 6. The three field variables φ, c and θ in a multi-dendrite simulation ($t = 33\tau = 22\ \mu s$)

and the error associated with the numerical evaluation of ρ_{tip}. Concentration peaks on the liquid side of the solid-liquid interface are due to solute segregation in the vicinity of dendrites (see concentration field in Fig. 3), i.e. there is little diffusion in the liquid compared to the rejection of atoms by the solid.

3.4 Tracking of crystal orientation in multi-dendrite simulations

Crystal orientation is implemented as explained in section 2.2. Fig. 6 shows the three field variables for the growth of two initial nuclei of size $4W_0$. The crystal orientation in the liquid is set to 0º, whereas the solid grains have crystal orientations of 30º and 60º. In this case, the simulation domain has a total size of 1.6 × 1.6 μm^2, and W_0 is fixed at 15.5 nm so that $W_0/d_0 = 10$.

4. Conclusions and Outlook

In this work, a phase-field model for dendritic solidification is applied to the ZnAlMg system, by treating it as a pseudo-binary dilute alloy. In addition to the phase transformation, the model gives the evolution of the solute concentration field and tracks the crystal orientation of the solidified grains. The latter is implemented with partial coupling, so that only surface tension anisotropy aspects of the solidification process be affected. 1D and 2D finite element simulations are performed with constant thermal undercooling and nuclei are introduced as initial conditions. The results are qualitatively consistent with analytical calculations of concentration profiles and growth velocity. To achieve convergence and quantitative validation of the results, a grid size of half the characteristic interface thickness is required, which limits the spatial domain of the simulations.

As the study aims at multi-dendrite solidification simulations of realistic dimensions for ZnAlMg coatings, subsequent work will include further parametric studies and the implementation of computational cost reduction techniques. A gain in accuracy should also be expected, if terms such as the “anti-trapping current”, the kinetic effects and the diffusion in the solid phase were considered. Furthermore, other thermal paths can be simulated to approximate real solidification conditions, as well as quasi-3D models to account for a greater variety of crystal orientations. These aspects and comparisons with experimental data will also be included and discussed in future work.

References

1. H. E. Chaieb, V. Maurel, K. Ammar, S. Forest, A. Tanguy, E. Héripré, F. Nozahic, J. -M. Mataigne, J. D. Strycker, In-situ localization of damage in a Zn-Al-Mg coating deposited on steel by continuous hot-dip galvanizing, *Scripta Materialia*, 243, 115960 (2024). Doi: https://doi.org/10.1016/j.scriptamat.2023.115960
2. M. Ahmadi, B. Salgın, B. J. Kooi, and Y. Pei, Genesis and mechanism of microstructural scale deformation and cracking in ZnAlMg coationgs, *Materials & Design*, 186, 108364 (2020). Doi: https://doi.org/10.1016/j.matdes.2019.108364
3. E. De Bruycker, Z. Zermout, and B. C. De Cooman, Zn-Al-Mg Coatings: Thermodynamic Analysis and Microstructure Related Properties, *Materials Science Forum*, 539–543, 1276 (2007). Doi: https://doi.org/10.4028/www.scientific.net/MSF.539-543.1276
4. E. Baril and G. L’Espérance, Studies of the morphology of the Al-rich interfacial layer formed during the hot dip galvanazing of steel sheet, *Metallurgical and Materials Transactions A*, 30, 681 (1999). Doi: https://doi.org/10.1007/s11661-999-1000-1
5. A. R. Marder, The metallurgy of zinc-coated steel, *Progress in Materials Science*, 45, 191 (2000). Doi: https://doi.org/10.1016/S0079-6425(98)00006-1
6. W. R. Osório, C. M. Freire, and A. Garcia, The effect of the dendritic microstructure on the corrosion resistance of Zn-Al alloys, *Journal of Alloys and Compounds*, 397, 179 (2005). Doi: https://doi.org/10.1016/j.jallcom.2005.01.035
7. C. Yaom, H. Teng, G. Jiang, Y. Li, M. Li, and G. Liu, The Solidification and Corrosion Behavior Determination of the Ti/B Added Zn-Al-Mg Alloys, *Journal of Alloys and Compounds*, 670, 239 (2016). Doi: https://doi.org/10.1007/s11595-022-2585-0
8. T. Prosek, J. Hagström, D. Persson, N. Fuertes, F. Lindberg, O. Chocholatý, C. Taxén, J. Šerák, D. Thierry, *Corrosion Science*, 110, 71 (2016). Doi: https://doi.org/10.1016/j.corsci.2016.04.022
9. W. R. Osório, C. M. Freire, and A. Garcia, The role of macrostructural morphology and grain size on the corrosion resistance of Zn and Al castings, *Materials Science and Engineering A*, 402, 22 (2005). Doi: https://doi.org/

10.1016/j.msea.2005.02.09

10. J. Elvins, J. A. Spittle, J. H. Sullivan, and D. A. Worsley, The effect of magnesium additions on the microstructure and cut edge corrosion resistance of zinc aluminium alloy galvanised steel, *Corrosion Science*, 50, 1650 (2008). Doi: https://doi.org/10.1016/j.corsci.2008.02.005
11. G. Jiang, L. Chen, H. Wang, and G. Liu, Microstructure and Corrosion Resistance Property of a Zn-Al-Mg Alloy with Different Solidification Processes, *MATEC Web of Conferences*, 109, 01004 (2017). Doi: https://doi.org/10.1051/matecconf/201710901004
12. S. Li, B. Gao, G. Tu, Y. Hao, L. Hu, and S. Yin, Study on the Corrosion Mechanism of Zn-5Al-0.5Mg-0.08Si Coating, *Journal of Metallurgy*, 2011, 917469 (2011). Doi: https://doi.org/10.1155/2011/917469
13. J. Tanaka, K. Ono, S. Hayashi, K. Ohsasa, and T. Narita, Effect of Mg and Si on the Microstructure and Corrosion Behavior of Zn-Al Hot Dip Coatings on Low Carbon Steel, *ISIJ International*, 42, 80 (2002). Doi: https://doi.org/10.2355/isijinternational.42.80
14. N. Provatas and K. Elder, Phase-Field Methods in Materials Science and Engineering, John Wiley & Sons (2011). Doi: https://doi.org/10.1002/9783527631520
15. A. Karma and W.-J. Rappel, Phase-field method for computationally efficient modelling of solidification with arbitrary interface kinetics, *Physical Review E*, 53, R3017 (1996). Doi: https://doi.org/10.1103/PhysRevE.53.R3017
16. B. Echebarria, R. Folch, A. Karma, and M. Plapp, Quantitative phase-field model of alloy solidification, *Physical Review E*, 70, 061604 (2004). Doi: https://doi.org/10.1103/PhysRevE.70.061604
17. J. C. Ramirez, C. Beckermann, A. Karma, and H.-J. Diepers, Phase-field modelling of binary alloy solidification with coupled heat and solute diffusion, *Physical Review E*, 69, 051607 (2004). Doi: https://doi.org/10.1103/PhysRevE.69.051607
18. H. Wang, X. Zhang, C. Lai, W. Kuang, and F. Liu, Thermodynamic principles principles for phase-field modelling of alloy solidification, *Current Opinion in Chemical Engineering*, 7, 6 (2015). Doi: https://doi.org/10.1016/j.coche.2014.09.004
19. T. Pinomaa, M. Lindroos, P. Jreidini, M. Haapalehto, K. Ammar, L. Wang, S. Forest, N. Provatas, and A. Laukkanen, *Philosophical Transactions of the Royal Society A*, 380, 20200319 (2022). Doi: https://doi.org/10.1098/rsta.2020.0319
20. C. Sarkis, 'Phase-field modeling of dendritic solidification for an Al-4.5wt%Cu atomized droplet using an anisotropic adaptive mesh', PhD. thesis, PSL University (2016). https://theses.hal.science/tel-01649221/
21. S. G. Kim, H.-S. Hwang, and J.-Y. Huh, Phase-field simulations of dendritic morphologies in hot-dip galvanized Zn-Al coatings, *Computational Materials Science*, 186, 110060 (2021). Doi: https://doi.org/10.1016/j.commatsci.2020.110060
22. E. De Bruycker, B. C. De Cooman, and M. De Meyer, Experimental study and microstructure Simulation of Zn-Al-Mg coationgs, *Revue de Metallurgie Paris*, 102, 543 (2005). Doi: https://doi.org/10.1051/metal:2005157
23. J. P. Mogeritsch, A. Ludwig, B. Böttger, G. Angeli, C. K. Riener, R. Ebner, *Proc. VII International Conference on Computational Methods for Coupled Problems in Science and Engineering (Coupled Problems 2017) Conf.*, pp. 1171 - 1182, (2017). https://smmp.unileoben.ac.at/fileadmin/shares/unileoben/smmp/docs/C161_Coupled_Problems_in_Science_and_Engineering_VII.pdf
24. Z. Guo and S. M. Xiong, On solving the 3-D phase field equations by employing a parallel-adaptive mesh refinement (Para-AMR) algorithm, *Computer Physics Communications*, 190, 89 (2015). Doi: https://doi.org/10.1016/j.cpc.2015.01.016
25. T. Z. Gong, Y. Chen, Y. F. Cao, X. H. Kang, and D. Z. Li, Fast simulations of a large number of crystals growth in centimeter-scale during alloy solidification via nonlinearly preconditioned quantitative phase-field formula, *Computational Materials Science*, 147, 338 (2018). Doi: https://doi.org/10.1016/j.commatsci.2018.02.003
26. Y. Chen, X. B. Qi, D. Z. Li, X. H. Kang, and N. M. Xiao, A quantitative phase-field model combining with front-tracking method for polycrystalline solidification of alloys, *Computational Materials Science*, 104, 155 (2015). Doi: https://doi.org/10.1016/j.commatsci.2015.04.003
27. J. A. Warren, R. Kobayashi, A. E. Lobkovsky, and W. C. Carter, Extending phase field models of solidification to polycrystalline materials, *Acta Materialia*, 51, 6035 (2003). Doi: https://doi.org/10.1016/S1359-6454(03)00388-4
28. R. Kobayashi and J. A. Warren, Modeling the formation and dynamics of polycrystals in 3D, *Physica A: Statistical Mechanics and its Applications*, 356, 127 (2005). Doi: https://doi.org/10.1016/j.physa.2005.05.024
29. H. Henry, J. Mellenthin, and M. Plapp, Orientation-field model for polycrystalline solidification with a singular coupling between order and orientation, *Physical Review B*, 86, 054117 (2012). Doi: https://doi.org/10.1103/Phys-

RevB.86.054117
30. T. Pusztai, G. Bortel, and L. Gránásy, Phase field theory of polycrystalline solidification in three dimensions, *Europhysics Letters*, 71, 131 (2005). Doi: https://doi.org/10.1209/epl/i2005-10081-7
31. M. Ahmadi, B. Salgın, M. Ahmadi, B. J. Kooi, and Y. Pei, Unraveling dislocation mediated plasticity and strengthening in crack-resistant ZnAlMg coatings, *International Journal of Plasticity*, 144, 103041 (2021). Doi: https://doi.org/10.1016/j.ijplas.2021.103041
32. S. Ghosh, 'Effects of solid-solid boundary anisotropy on directional solidification microstructures', PhD. thesis, Ecole Polytechnique (2015).
33. I. Ansara, A. T. Dinsdale, and M. H. Rand, 'COST 507 Thermochemical database for light metal alloys', European Commission (1998). https://www.opencalphad.com/databases/CGNA18499ENC_001.pdf
34. S. Yang, X. Su, J. Wang, F. Yin, N.-Y. Tang, Z. Li, X. Wang, Z. Zhu, H. Tu, and X. Li, Comprehensive Evaluation of Aluminum Diffusivity in Liquid Zinc, *Metallurgical and Materials Transactions A*, 42, 1785 (2011). Doi: https://doi.org/10.1007/s11661-010-0461-6
35. T. Gancarz, W. Gąsior, and H. Henein, Physicochemical Properties of Sb, Sn, Zn, and Sb-Sn System, *International Journal of Thermophysics*, 34, 250 (2013). Doi: https://doi.org/10.1007/s10765-013-1407-1
36. K. Keşlioğlu and N. Maraşli, Experimental determination of solid-liquid interfacial energy for Zn solid solution in equilibrium with the Zn-Al eutectic liquid, *Metallurgical and Materials Transactions A*, 35, 3665 (2004). Doi: https://doi.org/10.1007/s11661-004-0272-8
37. M. Erol, K. Keşlioğlu, and N. Maraşli, Measurement of Solid-Liquid Interfacial Energy for Solid Zn in Equilibrium with the ZnMg Eutectic Liquid, *Metallurgical and Materials Transactions A*, 38, 1539 (2007). Doi: https://doi.org/10.1007/s11661-007-9174-x
38. H. B. Aaron, D. Fainstein, and G. R. Kotler, Diffusion-Limited Phase Transformations: A Comparison and Critical Evaluation of the Mathematical Approximations, *Journal of Applied Physics*, 41, 4404 (1970). Doi: https://doi.org/10.1063/1.1658474
39. S. Kaboli, and J. R. McDermid, Effect of Process Variables on the Grain Size and Crystallographic Texture of Hot-Dip Galvanized Coatings, *Metallurgical and Materials Transactions A*, 45, 3938 (2014). Doi: https://doi.org/10.1007/s11661-014-2359-1
40. S. Vakili, I. Steinbach, and F. Varnik, On the numerical evaluation of local curvature for diffuse interface models of microstructure evolution, *Procedia Computer Science*, 108, 1852 (2017). Doi: https://doi.org/10.1016/j.procs.2017.05.256